

Structure and White Luminescence of Eu-Activated $(\text{Ba,Sr})_{13-x}\text{Al}_{22-2x}\text{Si}_{10+2x}\text{O}_{66}$ Materials

Grégoire Denis,[†] Philippe Deniard,[†] Eric Gautron,[†] Frédéric Clabau,[†] Alain Garcia,[‡] and Stéphane Jobic^{*,†}

Institut des Matériaux Jean Rouxel (IMN), UMR 6502 CNRS-Université de Nantes, 2 rue de la Houssinière, BP 32229, 44322 Nantes cedex 3, France, and Institut de Chimie de la Matière Condensée de Bordeaux (ICMCB), UPR 9048, 87 avenue du Dr. A. Schweitzer, 33608 Pessac cedex, France

Received November 14, 2007

The optical properties of Eu-activated $(\text{Ba,Sr})_{13-x}\text{Al}_{22-2x}\text{Si}_{10+2x}\text{O}_{66}$ materials have been determined after the structural reinvestigation of the hypothetical $\text{Ba}_{13}\text{Al}_{22}\text{Si}_{10}\text{O}_{66}$ material on the basis of the Gebert's model. The white fluorescence and phosphorescence of the $(\text{Ba,Sr})_{13-x}\text{Al}_{22-2x}\text{Si}_{10+2x}\text{O}_{66}:\text{Eu}$ series result from the existence of two broad emission bands associated with $^8\text{H}-4\text{f}^65\text{d}^1 \rightarrow ^8\text{S}-4\text{f}^7$ transitions peaking at 534 and 438 nm, the intensities of which may be tuned at room temperature via the control of the europium concentration and the substitution of Sr for Ba. This suggests the possibility to adjust the emission of the material to white LED requisites.

1. Introduction

Eu^{2+} -doped aluminates, silicates, aluminosilicates and derivatives are widely used in industry for their luminescent properties. Namely, the blue $\text{BaMgAl}_{10}\text{O}_{17}:\text{Eu}$ phosphor is designed for operation in flat panel displays (PDP),¹ Hg-free and Hg trichromatic lamps, and light-emitting diodes (LEDs); $\text{BaFCl}:\text{Eu}$ is employed to convert X-ray-absorbed beams into visible emission in photostimulable storage screens.² $\text{SrAl}_2\text{O}_4:\text{Eu,Dy,B}$ and $\text{CaAl}_2\text{O}_4:\text{Eu,Nd,B}$ are well-known for their green and blue long-lasting phosphorescence;^{3,4} $\text{SrB}_4\text{O}_7:\text{Eu}$ is included in suntanning lamp systems,⁵ and $\text{Sr}_2\text{P}_2\text{O}_7:\text{Eu}$ is a good candidate for therapeutic treatment of skin,⁶ etc. The great interest of all these materials lies in their efficient fluorescence in the visible spectrum, their chemical stability, and their easy synthesis route. Neverthe-

less, because of the constant and oppressing demand for phosphors with new or improved properties, the status of these materials is perpetually questioned.

Currently, a strong incentive is dedicated to potential phosphors for white-light UV-LED and to luminescence materials with long afterglow. Recently, we focused on the white phosphorescence of the europium-doped celcian- $\text{MAl}_2\text{Si}_2\text{O}_8$ compounds ($\text{M} = \text{Ca, Sr, Ba}$),^{7,8} while Yang et al. investigated the Eu- and Mn-coactivated $\text{CaAl}_2\text{Si}_2\text{O}_8$ prompted by their interest for white light phosphors for LED,⁹ and Li et al. reported the luminescence properties of Eu^{2+} -doped $\text{MAl}_{2-x}\text{Si}_x\text{O}_{4-x}\text{N}_x$ conversion phosphors for white LED applications.¹⁰ For all these $\text{MAl}_2\text{Si}_2\text{O}_8:\text{Eu}$ materials and their nitride derivatives, the emissions of Eu^{2+} cations are associated with $^8\text{H}-4\text{f}^65\text{d}^1 \rightarrow ^8\text{S}-4\text{f}^7$ transitions which extend on the whole visible range because of the existence of several available sites for the activators in the host lattice with different chemical environments. In the quest of new white phosphorescent materials, the study of the Eu-doped $\text{Ba}_{13-x}\text{Al}_{22-2x}\text{Si}_{10+2x}\text{O}_{66}$ aluminosilicates (hereafter abbreviated BASO:Eu) and its strontium derivatives

* To whom correspondence should be addressed. E-mail: stephane.jobic@cnrs-imn.fr. Fax: 33(0)2.40.37.39.95.

[†] Institut des Matériaux Jean Rouxel (IMN).

[‡] Institut de Chimie de la Matière Condensée de Bordeaux (ICMCB).

(1) Bizarri, G.; Moine, B. *J. Lumin.* **2005**, *113* (3–4), 199–213.

(2) Takahashi, K.; Miyahara, J.; Shibahara, Y. *J. Electrochem. Soc.* **1985**, *132* (6), 1492–1494.

(3) Matsuzawa, T.; Aoki, T.; Takeuchi, N.; Murayama, Y. *J. Electrochem. Soc.* **1996**, *143*, 2670–2673.

(4) Katsumata, T.; Nabae, T.; Sasajima, K.; Matsuzawa, T. *J. Cryst. Growth* **1998**, *183* (3), 361–365.

(5) Rattray, K. D.; Plante, L. J. U.S. Patent 4843279, 1989.

(6) Wilkens, J. H.; Stirne, R. U.S. Patent 6902563, 2002.

(7) Clabau, F. Ph.D. Thesis, Université de Nantes, Nantes, France, 2005.

(8) Clabau, F.; Garcia, A.; Bonville, P.; Gonbeau, D.; Le Mercier, T.; Deniard, P.; Jobic, S. *J. Solid State Chem.* **2008**, submitted for publication.

(9) Yang, W.-J.; Luo, L.; Chen, T.-M.; Wang, N.-S. *Chem. Mater.* **2005**, *17*, 3883–3888.

(10) Li, Y. Q.; de With, G.; Hintzen, H. T. *J. Electrochem. Soc.* **2006**, *153* (4), G278–G282.

(hereafter abbreviated Sr-BASO:Eu) has been initiated, and the influence of the Al/Si and Ba/Sr substitution on the structure and the optical properties is examined.

2. Experimental Section

2.1. Synthesis. (Ba,Sr)_{13-x}Al_{22-2x}Si_{10+2x}O₆₆ and (Ba,Sr)_{13-x}Al_{22-2x}Si_{10+2x}O₆₆:Eu polycrystalline samples were prepared through solid-state-reactions. Basically, barium carbonate (BaCO₃ 99.997% Alfa Aesar), strontium carbonate (SrCO₃ 99.99% Alfa Aesar), alumina γ (Al₂O₃ 99.997% Alfa Aesar), silica (SiO₂ 99.99% Chempur), and europium oxide (Eu₂O₃ 99.99% Alfa Aesar) were weighed in the appropriate proportions. Hereafter, Eu (and Sr) doping percentages will refer to an ideal and hypothetical Ba₁₃Al₂₂Si₁₀O₆₆ formula, that is, BASO:Eu1% will correspond for instance to the targeted Ba_{12.87}Eu_{0.13}Al₂₂Si₁₀O₆₆ composition. In the particular case of low doping (lower than to 0.04% of europium), europium was introduced as a solution with europium nitrate (Eu(NO₃)₃ 99.99% Rhodia) dissolved in distilled water. Starting materials were ball milled with a Fritsch Pulverisette 7 for 7 h in silicon nitride container 70% filled with ethanol. Then, after drying in a stove at 150 °C, the blends were calcined at 1350 °C for 30 h in alumina crucibles in a reducing argon/hydrogen (95/5%) atmosphere in a horizontal tube furnace. The reducing atmosphere was replaced by air when stabilization of Eu³⁺ cations was desired. Higher synthesis temperatures are prohibited because of the noncongruent fusion at 1460 °C.¹¹ Each material underwent a second firing in similar conditions after an intermediate grinding step. At this stage, let us mention that attempts to prepare Ba₁₃Al₂₂Si₁₀O₆₆ with an exact Al/Si molar ratio of 2.2 systematically lead to BaAl₂O₄ as byproduct. Then, silica excess compositions with Al/Si molar ratio of 2.00 (22/11.0), 1.91 (22/11.5), 1.83 (22/12.0), and 1.76 (22/12.5) were explored, leading to the conclusion that (i) the BaAl₂O₄ or BaAl₂Si₂O₈ phases were systematically detected by X-ray diffraction as side-products for Al/Si ratio of 2.0 and 1.76, respectively; (ii) a single BASO:Eu phase could be obtained for Al/Si ratio of 1.91 when europium doping was higher than 2% (For lower europium concentration, Rietveld refinements highlighted that the BaAl₂O₄ phase is present with a weight percentage inferior than 2.5%); (iii) undoped or slightly doped single phases were only obtained for a Al/Si ratio of 1.83. In the following, compounds prepared with a Al/Si of 1.83 will be labeled R-BASO (R as abbreviation for rich), while compounds prepared with a Al/Si ratio of 1.91 will be labeled P-BASO (P as abbreviation for poor). Sr-BASO:Eu1% materials were prepared as a single-crystalline phase with an Al/Si ratio of 1.91 up to a Sr/Ba substitution rate of 60% (i.e., Sr_{7.80}Ba_{5.07}Eu_{0.13}Al₂₂Si₁₀O₆₆). For richer strontium compositions, Sr₂Al₂SiO₇ or SrAl₂Si₂O₈ phases were always present as impurity. Currently, the existence of the totally substituted “Sr₁₃Al₂₂Si₁₀O₆₆” phase has been detected from XRD analysis, but its synthesis yield has to be significantly enhanced to undertake proper characterizations of its physical properties.

2.2. Powder X-Ray Diffraction. X-ray diffraction (XRD) measurements were performed on a D8 Bruker diffractometer employing the CuK–L₃ radiation (germanium monochromator) and a Vantec multigap detector in the 5–110° 2 θ interval. To verify the purity of prepared samples, the XRD powder patterns were systematically compared to the calculated ones of Ba₁₃Al₂₂Si₁₀O₆₆ (ICSD 2940), BaAl₂O₄ (ICSD 75427), Sr₂Al₂SiO₇ (ICSD 30698), and SrAl₂Si₂O₈ (ICSD 4354). Moreover, structure refinements based

Table 1. Instrumental Parameters of the D8 Bruker Diffractometer Used for Rietveld Refinements of BASO and SrBASO Materials and Their Eu-Doped Derivatives

primary and secondary radius	217.5 mm
receiving slit width	0.1 mm
reception slit divergence angle	0.2°
primary Soller slit aperture	2.5°
source and sample length	12 mm
receiving slit length	16 mm

on Gebert's crystal investigations¹² were carried out with the Jana2006 Beta version software,¹³ using a Rietveld procedure with the fundamental parameter approach in the *P*6₃ space group.¹⁴ This method made possible the deconvolution of the X-ray line profile taking into account the intrinsic broadenings associated with the diffractometer (X-ray energy dispersion and optics) and the specimen itself. Namely, the CuK–L₃ emission profile was calculated from the physics data collected by Cheary et al. and the monochromator setting.¹⁴ The instrumental function was expressed in terms of the geometry of the diffractometer with the relevant parameters reported in Table 1. The only refined function concerned the specimen itself, that is, the crystallite size (Å) and microstrains (%). The maximum crystal size that can be accurately determined with the diffractometer resolution we used was estimated to be 2000 Å. The refinement procedure was composed of the calculation of the background (Legendre polynomials), followed by the computation of the sample displacement, cell parameters, crystallite sizes, and microstrains. The absorption resulting from roughness was then evaluated prior to the Rietveld refinement of the atom positions. Atomic displacement parameters were constrained to be identical within a given atomic species (i.e., O, Al/Si, Ba). Finally, the Ba3 site occupation fraction was freed, with Ba1 and Ba2 sites being kept fully occupied. Fourier difference maps were calculated to ensure the structure validity, and the structure refinement was stopped when the electronic residue ranged within the [−1; +1] e/Å³ interval. Bond valence calculations were carried out according to the Brown and Altermat theory.^{15,16}

2.3. Electron Diffraction. Selected area electron diffraction (SAED) was performed on a Philips CM30 transmission electron microscope operating at 300 kV to obtain tilt series. The position and intensity of each diffraction spot from each electron diffraction pattern were determined and refined by the program system ELD from Calidris publisher. These data were input into the Trice software (Calidris) with the direction of the tilt axis and the angle of tilt.¹⁷ After reconstruction of the 3D reciprocal lattice, the unit cell parameters and the lattice type were extracted.

2.4. Helium Pycnometry. Powder densities have been evaluated with a Micromeritics Accupyc 1330 equipment.

2.5. Optical Measurements. Optical measurements were done using a fluorescence spectrophotometer Fluorolog-3 (Jobin Yvon) with a xenon lamp as excitation source. Emission and excitation spectra were corrected for the monochromator response, detector sensibility, and lamp intensity. The quantum efficiency was calculated from the luminescence of a standard Zn₂SiO₄:Mn which

(11) Oehlschlegel, V. G.; Kockel, A.; Biedl, A. *Glastech. Ber.* **1974**, *47*, 31–41.

(12) Gebert, W. Z. *Kristallogr.* **1972**, *135*, 437.

(13) Petricek, V.; Dusek, M.; Palatinus, L. *The Crystallographic Computing System JANA*, 2006 Beta; Academy of Sciences: Praha, Czech Republic, 2006.

(14) Cheary, R. W.; Coelho, A. A. *J. Appl. Crystallogr.* **1992**, *25*, 109–121.

(15) Brese, N. E.; O'Keefe, M. *Acta Crystallogr.* **1991**, *B47*, 192–197.

(16) Brown, I. D. *Acta Crystallogr.* **1995**, *B48*, 553–572.

(17) Zou, X. D.; Hovmöller, S. In *Trice—A Program for Reconstructing 3D Reciprocal Space and Determining Unit Cell Parameters* Proceedings of the XVIIIth IUCr Congress & General Assembly, 1999; Industry & University Cooperative Research Program: Arlington, VA, 1999; p 205.

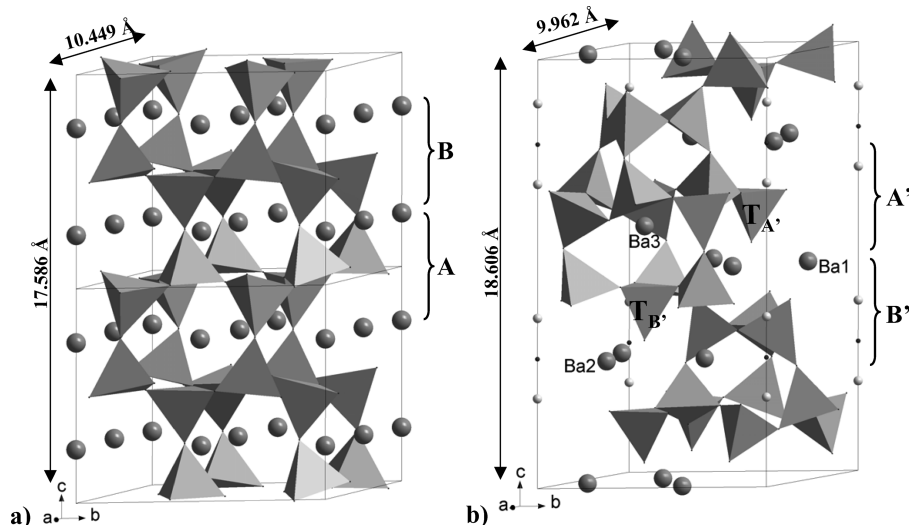


Figure 1. (a) BaAl_2O_4 structure represented in the $a \times a \times 2c$ supercell. (b) $\text{Ba}_{13-x}\text{Al}_{22-2x}\text{Si}_{10+2x}\text{O}_{66}$ structure according to Gebert.¹² The A, B tetrahedra layers for BaAl_2O_4 and the A', B' tetrahedra ones for BASO are indicated by braces.

exhibits an external quantum efficiency of 0.66 at the exciting wavelength of 250 nm. The low-temperature spectrum was carried out with a homemade cryostat at the liquid nitrogen temperature. The long afterglow decay was performed after a 5 min excitation at 324 or 278 nm. The spectra decomposition and emission decay fit were accomplished with the Origin 7.5 software (OriginLab Corporation, U.S.A.).

3. Results

3.1. Crystal Structure. On the basis of thermodynamical investigations, Oehlschlegel et al. underlined the capacity of BaAl_2O_4 to incorporate SiO_2 with release of Al_2O_3 to form BASO.¹¹ This assertion implies that the structure of $\text{Ba}_{13}\text{Al}_{22}\text{Si}_{10}\text{O}_{66}$ might be described as a derivative of the BaAl_2O_4 structure, that is, a structure built upon the tridimensional packing of 4-folded corner-shared $[\text{AlO}_4]$ tetrahedra (Figure 1a) with barium in 7-, 8-, and 9-fold coordination. Namely, the BaAl_2O_4 substructure can be decomposed in two $^{2/\infty}[\text{Al}_8\text{O}_{12}]$ slabs, labeled A and B, stacked along the c -axis of an hexagonal cell. Each slab consists of a $^{2/\infty}[\text{Al}_4\text{O}_8]$ layer with four tetrahedra pointing toward the $+c$ direction and a $^{2/\infty}[\text{Al}_4\text{O}_8]$ sublayer with four tetrahedra pointing toward the $-c$ direction, with the basal planes of the $[\text{AlO}_4]$ lying roughly in the (a,b) plane. Slabs A and B are identical and crystallographically related via a 6_3 operation, and their condensation results in the appearance of head-to-foot tetrahedra $[\text{Al}_2\text{O}_7]$ entities. In a first approximation, the BASO structure, with 32 $[\text{TO}_4]$ tetrahedra ($T = \text{Al}, \text{Si}$) per unit cell, may be viewed as deriving from the BaAl_2O_4 structure, with 16 $[\text{AlO}_4]$ per unit cell, by a doubling of the c -parameter (Figure 1b). The structure may be decomposed in two types of slabs, labeled A' and B', whose compositions are $^{2/\infty}[\text{Al}_4\text{Si}_4\text{O}_{16}]$ and $^{2/\infty}[\text{Al}_7\text{SiO}_{16}]$, respectively, according to Gebert. A' slabs exhibit features similar to those of the A slabs in BaAl_2O_4 with location of silicon and aluminum in two distinct sublayers. Moreover, because of the substitution of Al for Si ($r(\text{Si}^{4+}) = 0.26$,

$r(\text{Al}^{3+}) = 0.39$),¹⁸ some distortions of the network are generated, and triangular six-tetrahedra ring cavities in A (Figure 2a) are replaced by hexagonal and rectangular six-tetrahedra ring cavities in A' (Figure 2b). Moreover, let us mention that one $[\text{SiO}_4]$ tetrahedron of A' slab, named $T_{A'}$, remains 3-fold coordinated, even when slabs A' and B' are condensed in a 3D packing. B' slabs may be described from the B model via the following transformations. Let us consider a B slab with $[\text{AlO}_4]$ polyhedra in blue and green depending on whether they point toward $-c$ or $+c$ (Figure 2c). The $^{2/\infty}[\text{Al}_7\text{SiO}_{16}]$ double layer of BASO may be then generated by application of the following operations: (i) removal of one Al^{3+} cation as schematized in Figure 2d, (ii) rearrangement of the three blue polyhedra surrounding the formed vacancy into a $[\text{Al}_3\text{O}_9]$ conglomerate (i.e., three $[\text{AlO}_4]$ sharing apexes, Figure 2e) linked to green tetrahedra by corner sharing, and (iii) reintroduction of the previously expelled tetrahedron as a $[\text{SiO}_4]$ one, labeled $T_{B'}$, connected to three green $[\text{AlO}_4]$ polyhedra, (Figure 2e). The defined layers show three and seven corner-sharing tetrahedra voids with one 3-fold coordinated tetrahedron ($T_{B'}$) (Figure 2f). The aluminate skeleton of the BASO structure is then reconstructed from the condensation of slabs A' and B' along c leading to the infinite sequence $-\{^{2/\infty}[\text{9O}]-^{2/\infty}[\text{4Si}]-^{2/\infty}[\text{8O}]-^{2/\infty}[\text{4Al}]-^{2/\infty}[\text{9O}]-^{2/\infty}[\text{4Al}+1\text{Si}]-^{2/\infty}[\text{8O}]-^{2/\infty}[\text{3Al}]\}-$. This structural rearrangement goes along with a contraction and stretching of the a and c parameters, respectively.

The BASO structure contains three crystallographically different barium sites labeled Ba1, Ba2, and Ba3 at a $6c$, $6c$, and $2b$ Wyckoff positions, respectively (Figure 3). On the basis of the structure determination of Gebert,¹² Ba1, Ba2, and Ba3 cations are 8-fold, 7-fold, and 9-fold coordinated with an average Ba—O distance of 2.88, 2.82, and 2.87, respectively. To ensure the right charge balance, Gebert proposed that the $2b$ site (Ba3) is half-occupied even though the crystal structure refinement concluded a 33% occupancy

(18) Shannon, R. D. *Acta Crystallogr.* **1976**, A32, 751.

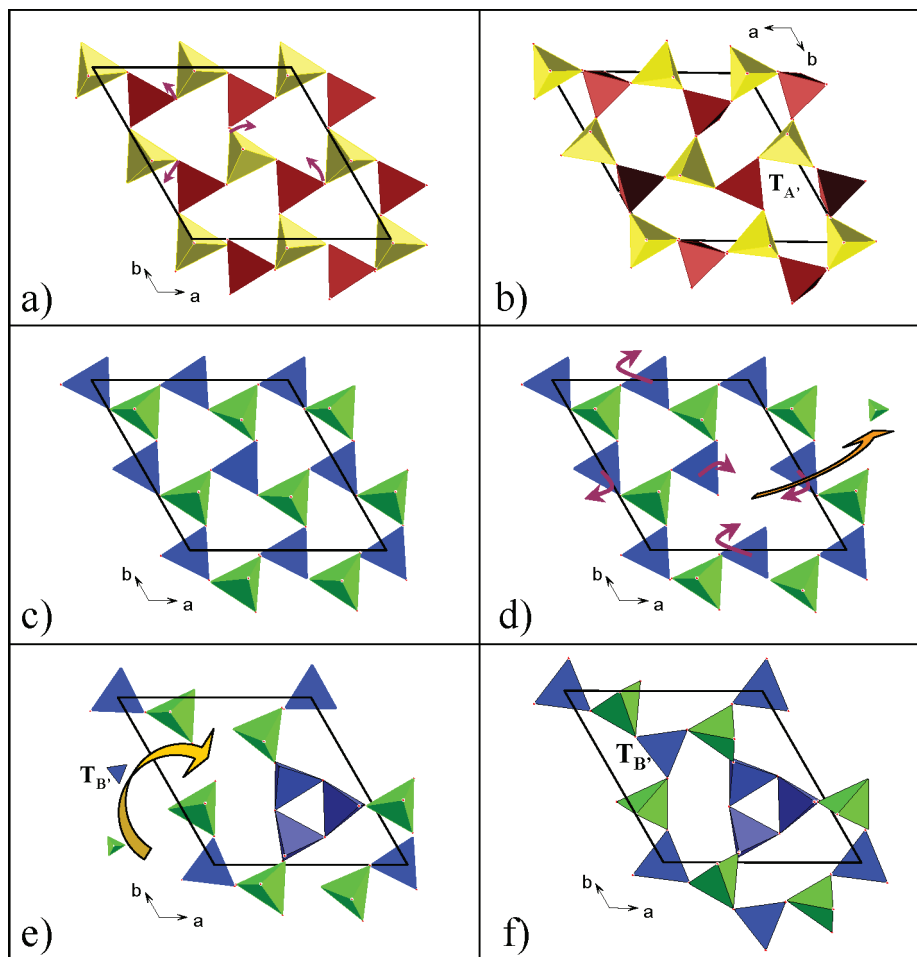


Figure 2. (a) A layer of BaAl_2O_4 with arrows indicating how tetrahedral shift from a to b. (b) A' layer of BASO. (c) B layer of BaAl_2O_4 . (d) B' layer of BASO obtained from the removal of a green tetrahedron from the B layer. Arrows indicate the relaxations of the blue tetrahedra which gives rise to e. (e) The previously removed green tetrahedron is added in the remaining free space. (f) Final B' layer of BASO.

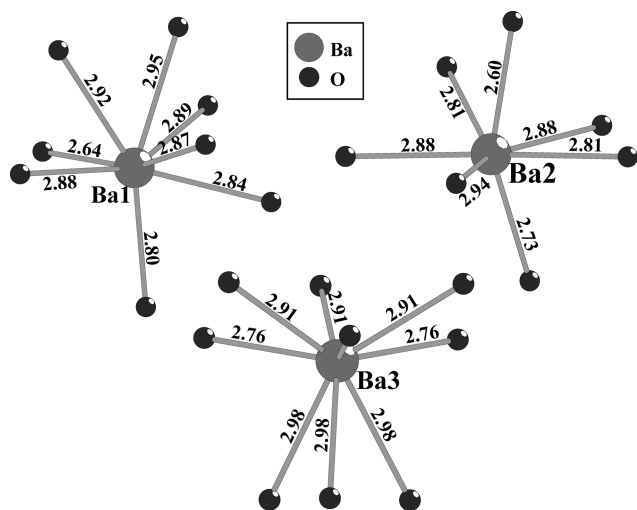


Figure 3. Barium environment of the BASO structure with Ba–O distances (in Å) issued from the R-BASO Rietveld refinement.

factor, suggesting a slightly more intricate chemical composition. This prompted us to embark on the structural reinvestigation of the BASO structure. In this framework, SAED tilt series along $[001]$ direction were first undertaken. The experimental patterns coincided with the simulated ones using the Gebert's model (SG: $P6_3$). The cell parameters

obtained with Trice ($a = 10.1 \text{ Å}$, $b = 10.0 \text{ Å}$, $c = 18.5 \text{ Å}$, $\alpha = 91^\circ$, $\beta = 89^\circ$, $\gamma = 119^\circ$) are very similar to those found by Gebert and match an hexagonal symmetry within angle uncertainties. No superstructure was evidenced, the extra peaks observed in Figure 4 being associated with double diffraction caused by the thickness of the crystal. Second, the Rietveld analyses of the X-ray patterns of prepared materials (Table 2) were then carried out to address the barium nonstoichiometry problem, the aluminum/silicon ordering, and the influence of doping and substitution on the BASO structure type. For the R- and P-BASO investigated compositions, a Rwp factors of about 6.5% was achieved with Fourier difference electronic residues ranging from ~ -1.05 and $\sim +0.50 \text{ e}^-/\text{Å}^3$. In contrast, the exact stoichiometry of Sr-BASO structure cannot be deduced from Rietveld refinement because (i) a high correlation is expected between the heaviest elements in the structure (Sr, Ba) and the Rietveld scale factor and because (ii) the strontium atom is supposed to sit in all the barium sites leading to the impossibility to dispatch the electron density between the two species and vacancies.

Despite the large number of peaks but because of the use of the fundamental parameter approach, these Rwp and electronic values attest to the reliability of the fitting

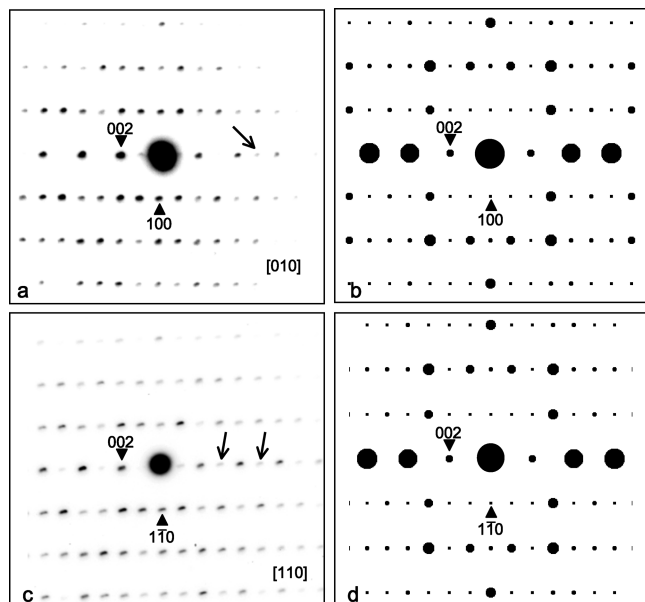


Figure 4. (a) Experimental and (b) simulated electron diffraction patterns (EDP) of BASO along the [010] zone axis. (c) Experimental and (d) simulated EDP of BASO along the [110] zone axis. Arrows indicate double diffraction spots. Simulations were carried out from the Gebert's model.

Table 2. Relevant Results of the Rietveld Refinement of Undoped BASO with Different Al/Si Ratio^a

	R compound	P compound
BaAl ₂ O ₄ (wt %)	0	2.5
Rwp (%) / Berar factor	6.80/1.80	6.26/1.88
<i>a</i> / <i>c</i> (Å)	9.96245(9)/18.6065(2)	9.9635(9)/18.6206(2)
<i>U</i> (Ba)/ <i>U</i> (Al/Si)	0.0084(7)/0.0010(16)	0.0151(6)/0.0028(15)
<i>U</i> (O)	0.004(2)	0.011(2)
SOF(Ba3)	0.168(7)	0.223(6)
Ba/formula	12.34(2)	12.44(2)
strain (%)	20(1)	25(1)
Fourier min and max density (e ⁻ /Å ³)	-1.00(on Ba2)/+0.50	-1.04(on Ba2)/+0.59

^a Rwp = weighted profile residual factor, *U* (Å²) = atomic displacement parameter, SOF = site occupation fraction. Atomic position are given in Supporting Information.

procedure and the overall validity of the crystal structure. Crystal sizes were found to be too high to lead to profile widening. Moreover, regardless of the studied sample, the peak profile refinements lead to a microstrain percentage of about 20%, probably in relation with the random occupancy of Ba3 site and the possible statistical substitution of Al³⁺ for Si⁴⁺ and vice versa, as debated below.

3.1.1 Ba Nonstoichiometry. For the R and P undoped compounds, the Rietveld refinement of the Ba3 site occupancy systematically lead to a value inferior to 0.25 instead of the 0.50 value requested to balance the charges of a $3/_{\infty}[\text{Al}_{22}\text{Si}_{10}\text{O}_{66}]^{13-}$ aluminosilicate framework (Table 2). Namely, for samples with nominal Al/Si ratio of 1.83 and 1.91, the overall composition of BASO issued from XRD analyses should be written Ba_{12.34(2)}M₃₂O₆₆ and Ba_{12.44(2)}M₃₂O₆₆ (M = Al, Si) with a partial substitution of Al³⁺ for Si⁴⁺ compared to the ideal Al/Si ratio of 22/10. Actually, the replacement of a [AlO₄]⁵⁺ tetrahedron by a [SiO₄]⁴⁺ tetrahedron will generate cationic vacancies according to $2\text{Al}^{3+} \rightarrow 2\text{Si}^{4+} + \text{V}_{\text{Ba}}^{''}$ substitution. Consequently, this excludes the long-range Si/Al-ordering model proposed

Table 3. Bond Valence of Main Group Elements in Tetrahedral Site in BASO

sites	site attribution ICSD 2940	multiplicity of site	valence		connectivity
			R-BASO	P-BASO	
T ₁ –T _{B'}	Si	2	3.80	3.70	T5 T5 T5 (Ba2)
T ₂	Si	6	3.45	3.39	T4 T4 T5 T7
T ₃ –T _{A'}	Si	2	3.80	3.60	T4 T4 T4 (Ba1)
T ₄	Al	6	3.23	3.26	T2 T2 T3 T8
T ₅	Al	6	2.59	2.68	T1 T2 T6 T6
T ₆	Al	2	2.92	3.50	T5 T5 T5 T7
T ₇	Al	2	3.30	2.80	T2 T2 T2 T6
T ₈	Al	6	3.10	3.23	T8 T8 T4 T5

by Gebert at the benefit of a disordered one. On the basis of the aforementioned structural description, the number of silicon and aluminum tetrahedra remains fixed to 32 per unit cell. As a consequence, the overall BASO formula may be written Ba_{13–x}Al_{22–2x}Si_{10+2x}O₆₆, that is, Ba_{12.34}Al_{20.68}Si_{11.32}O₆₆ and Ba_{12.44}Al_{20.88}Si_{11.12}O₆₆ for R- and P-BASO, respectively. The calculated densities for such compositions (i.e., 3.77 and 3.78 g cm⁻³, respectively) are in good agreement with Pycnometer measurements (3.77 and 3.77 g cm⁻³, respectively) which assert the proposed stoichiometries.

3.1.2 Aluminum/Silicon Ordering. Experimentally, going from poor to rich SiO₂ samples, a reduction of the *c* cell parameter is observed, while the *a* parameter remains almost constant (Table 2). The decrease of the *c* cell parameter may be explained by the smaller radius of Si⁴⁺ cations compared to Al³⁺ ones and the lower occupancy of the Ba3 site when Si concentration is enhanced. For unknown reasons, these factors will affect the *c* parameter only. In Table 3, the calculated valence bonds of the undistinguished Si and Al main group element in tetrahedral sites issued from the Rietveld analysis of the X-ray patterns are reported. Namely, the 32 [MO₄] tetrahedra of the BASO structure are associated with eight crystallographic sites labeled T₁ (= T_{A'}), T₂, T₃ (= T_{B'}), T₄... and T₈ assigned to Si₁, Si₂, Si₃, Al₁, ... Al₅ according to the notation used by Gebert, respectively. The T_{A'}, T₂, and T_{B'} sites exhibit the higher valences of the eight tetrahedral sites, that is, 3.75, 3.42, and 3.70, respectively, which assert their original attribution to silicon by Gebert. The valence of sites T₄–T₈ tends toward lower values, suggesting that these sites are mainly occupied by Al³⁺ cations. Consequently, even if Si⁴⁺ and Al³⁺ cations are expected to be randomly dispatched over sites T₁–T₈, Si atoms lie preferentially on sites T_{A'}, T₂, T_{B'}, while aluminum atoms lie preferentially on sites T₄–T₈. This distribution agrees with NMR studies carried out on gehlenite Ca₂Al₂SiO₇ and melilite Sr₂Al₂SiO₇, which show the preferential occupancy by Si⁴⁺ cations of tetrahedra sharing only three corners with its surrounding at the expense of Al³⁺ cations.¹⁹ Nonbridging T_{A'} and T_{B'} tetrahedral sites can thus be alleged to be fully occupied by silicon. Moreover, the valence of the T₂ site is significantly lower than that for the T_{A'} and T_{B'} site. This could be the signature of a significant occupancy of this site by aluminum.

3.1.3 Eu Doping and Ba/Sr Substitution. Under a reducing and oxidant thermal treatment atmosphere, the

(19) Capron, M. Ph.D. Thesis, Université d'Orléans, Orléans, France, 2001.

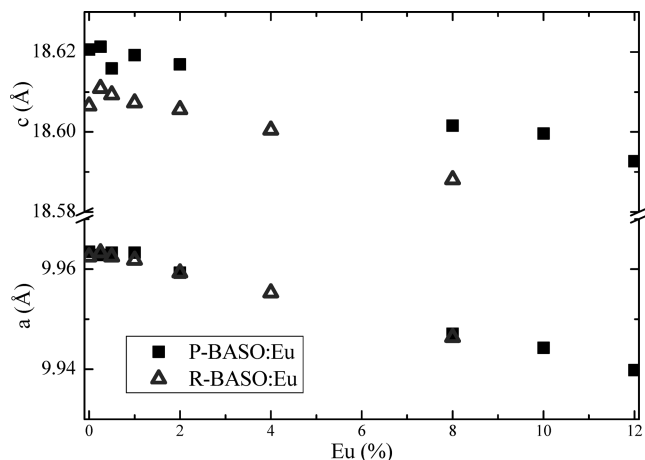


Figure 5. Evolution of the cell parameters of P-BASO:Eu (■) and R-BASO:Eu (○) with Eu concentration.

barium cation can be substituted for europium, strontium, or both. In all case, a solid solution is observed because the evolution of the cell parameters of P- and R-BASO with the Eu concentration respects a Vegard law (Figure 5).

3.2. Fluorescence and Phosphorescence. Except where indicated, only the optical properties of Eu doped R-BASO materials, that is, samples free of BaAl_2O_4 impurities, are discussed hereafter.

3.2.1 Fluorescence of BASO:Eu Prepared in Air. For europium-doped compounds synthesized in air, the photoluminescence spectra, with excitation at 254 or 324 nm, reveal one broadband peaking at 420 nm and multiple sharp emission peaks at 578, 591, 614, 654, and 704 nm, with shoulders at 597, 627, and 691 nm (Figure 6). Specifically, a second very wide band centered around 535 nm is suspected under excitation at 324 nm. For all investigated samples, no long afterglow is perceptible with naked eyes, and the fluorescence is white-pink in agreement with the major presence of Eu^{3+} . Nevertheless, some Eu^{2+} cations are present as traces, the large bands being associated with $\text{Eu}^{2+}4f^65d^1 \rightarrow 4f^7$ transitions (vide supra). The sharp peaks can be explained in terms of internal $\text{Eu}^{3+}4f \rightarrow 4f$ transitions. Hence, the intense emissions at 614 and 704 nm are attributed to the $^5D_0 \rightarrow ^7F_2$ and $^5D_0 \rightarrow ^7F_4$ transitions, respectively, with shoulders arising most likely from the random distribution of Eu^{3+} cations at different Ba sites. The peaks at 578, 591, and 654 nm are assigned to $^5D_0 \rightarrow ^7F_0$, $^5D_0 \rightarrow ^7F_1$, and $^5D_0 \rightarrow ^7F_3$ radiative returns, respectively. Since transitions with $\Delta J = \pm 2$ are predominant, it may be concluded that Eu^{3+} cations occupy sites with no inversion center,²⁰ which is consistent with the aforementioned structural description of BASO. The excitation spectrum at the emission wavelength of 614 nm (insert in Figure 6), in the 350–550 nm range, consists of thin peaks located at 360, 380, 393 (with a shoulder at 400 nm), 413, 463, and 528 nm corresponding to spin and symmetry forbidden $^7F_0-4f^6 \rightarrow ^5D_J-4f^6$ transitions. An intense excitation appears at higher energy around 260 nm because of the charge transfer. More specifically,

on the basis of the excitation spectrum at the emission wavelength of 535 nm, the bump at 320 nm would be associated with the preferential excitation of Eu^{2+} cations.

3.2.2 Fluorescence of BASO:Eu Prepared under H_2/Ar Atmosphere. Materials prepared under a reducing atmosphere exhibit a bright white fluorescence for Eu doping up to 4%, and a yellow-greenish fluorescence for higher Eu concentration. An afterglow which may last several minutes is systematically observed for all compositions reported here. Namely, the photoluminescence spectra of BASO:Eu compounds reveal, at first sight, two large $4f^65d \rightarrow 4f^7$ bands centered at 534 and 438 nm with a quantum efficiency estimated at about 0.70 from measurements on the R-BASO:Eu2% compounds at $\lambda_{\text{exc}} = 324$ nm. The relative ratio of these blue-violet emission (438 nm) and green emission (534 nm) strongly depends upon the excitation wavelength (Figure 7) and the Eu concentration (Figure 8). Briefly, the blue-violet fluorescence is favored over the green one when excitation is shifted from 250 to 278 nm and when the Eu-doping rate decreases from 8% to 0.04%. Moreover, the fitting of the emission spectra of a R-BASO:0.04%Eu sample collected at 100K via Gaussian curves (based on a configurational coordinate model with a strong electron–lattice coupling) requires the account for three emissions positioned at 2.96 (419 nm), 2.81 (442 nm), and 2.26 eV (549 nm) with full width at half-maximum of 0.24, 0.34, and 0.59 eV, respectively (insert in Figure 7). These three bands, hereafter labeled GA, GB, and GC, are associated with divalent EuA, EuB, and Euc cations distributed over the three alkaline earth sites of BASO (and Sr-BASO). The assignment of an emission to an europium in a given crystal site, that is, Ba1, Ba2, or Ba3, will be discussed below. Let us mention here that the decomposition of the two bands GA and GB are strongly correlated. Thus, only the total (GA + GB) emission intensity will be discussed in the following. Emissions associated with europium III are never detected.

The excitation spectrum of R-BASO:Eu2% displayed in Figure 7 is composed of a broadband spreading from 440 to 240 nm. At least five distinct bands may be perceived, the green emission (GC) being preferentially excited at 3.27 (380 nm), 3.88 (320 nm), and 4.97 eV (250 nm) and the blue one (GA + GB) at 3.34 (372 nm), 3.88 (320 nm), and 4.49 eV (276 nm). A significant overlap exists between the excitation and emission spectra, suggesting that energy transfers may occur from EuA and EuB cations toward Euc cations. Because of the electron dipole–dipole interaction character of the transition, transfers may occur for Eu–Eu distances as long as 30 Å (i.e., for doping rate higher than $\sim 0.04\%$) and are favored when the temperature is raised.²⁰ On the basis of the Förster–Dexter theory,^{21,22} the critical distance in BASO:Eu between two Eu^{2+} cations leading to energy transfer can be estimated from the $R_c^6 = 0.63 \times 10^{28} \times [(4.8 \times 10^{-16} \times P)/E^4] \times \text{SO}$ formula, which ends at a critical distance of 18 Å for an oscillator strength P of 0.01 (Ce^{3+} oscillator

(20) Blasse, G.; Grabmaier, B. C. *Luminescent Materials*; Springer Verlag: Berlin, 1994.

(21) Förster, T. *Ann. Phys.* **1948**, 2, 55.

(22) Dexter, D. L. *J. Chem. Phys.* **1953**, 21 (5), 836–850.

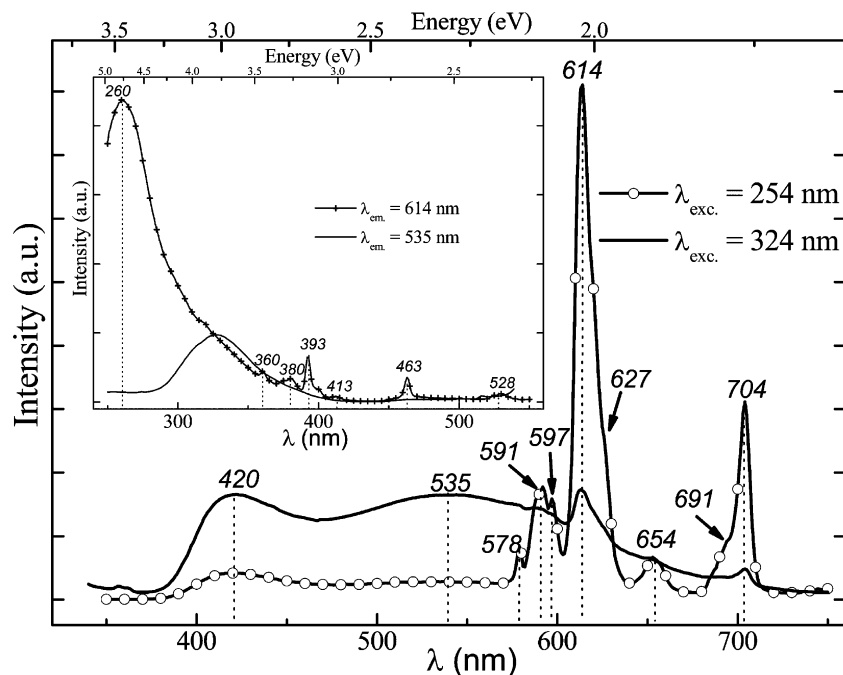


Figure 6. Emission spectra ($\lambda_{\text{exc}} = 254$ and 324 nm) of R-BASO:Eu2% thermally treated under air atmosphere. Insert: Excitation spectra ($\lambda_{\text{em}} = 614$ and 535 nm).

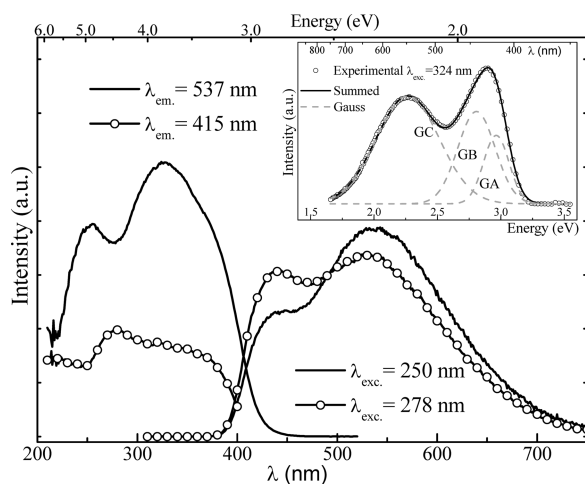


Figure 7. Emission and excitation spectra of R-BASO:Eu2%. Insert: Gaussian decomposition of the emission spectrum of R-BASO:Eu0.04% collected at 100 K and $\lambda_{\text{exc}} = 324$ nm.

strength used as reference),²³ a spectral overlap integral SO of 0.11 eV^{-1} and an energy at the maximum overlap E of 3.20 eV . Consequently, if Eu cations are randomly distributed, energy transfer should be observed, a priori, for europium rates higher than 0.30% (vide supra). This value has to be considered as indicative because of the sixth power of the equation.

To shed some light on the evolution of the luminescence spectrum with Eu concentration, low-temperature measurements were carried out on BASO:Eu1%. Results are displayed in Figure 9. Namely, the intensity of the blue-violet emission (GA + GB) undergoes a 15% decrease from liquid nitrogen (LN) to room temperature (RT), while the intensity of the green (Gc) emission undergoes a 40% increase. This goes along with a blue shift of the Gc band, probably related

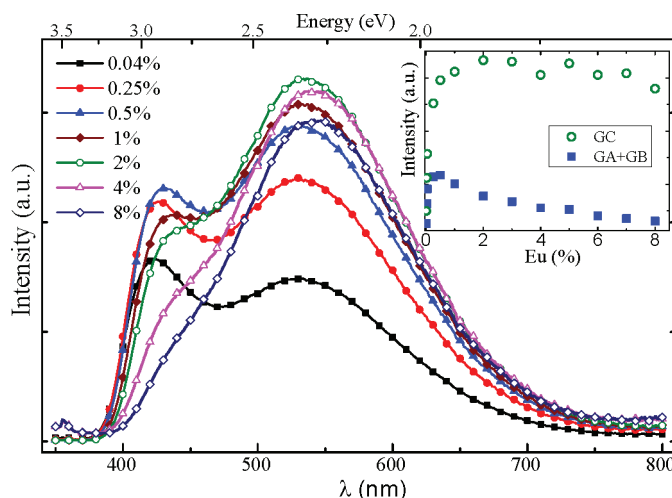


Figure 8. Emission spectrum of BASO:Eu ($\lambda_{\text{exc}} = 324$ nm) for Eu concentration ranging from 0.04% to 8% . Insert: Evolution of GA + GB and Gc intensities with Eu concentration.

to the elongation of the Eu–O interatomic distance, which favors a lower splitting of the Eu d-block. In the framework of the classical 1D-configuration model, thermal quenching is enhanced when the parabola offset, ΔR , related to the emission width, is increased. Thus, Eu cations should be more affected than the EuA and EuB ones by a decrease of its emission with temperature. The opposite is observed because the thermal quenching of Gc is, most likely, highly compensated by the thermally activated energy transfers from EuA and EuB toward EuC. The energy transfers also explain the evolution of the emission intensities with the europium concentration at room temperature (Figure 8). The intensity of the three bands increases up to an europium rate of 0.12% (see insert in Figure 8) that indicates that the aforementioned, estimated critical concentration is overestimated. Beyond this concentration and up to $\sim 3\%$, the GA and GB emissions are

(23) Blasse, G. *Philips Res. Rep.* **1969**, *24*, 131–144.

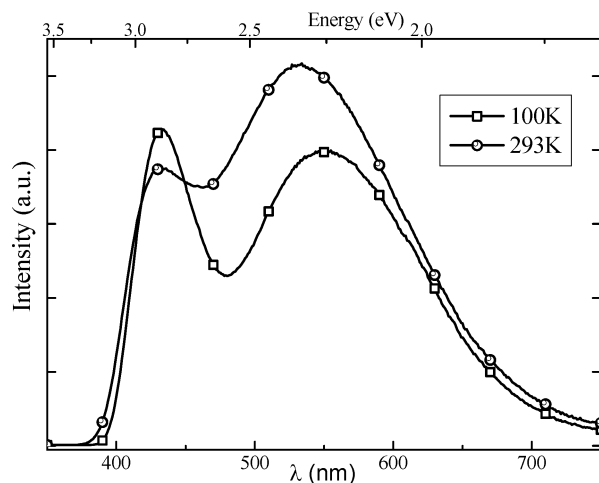


Figure 9. Emission spectrum of BASO:Eu1% ($\lambda_{\text{exc}} = 254$ nm) performed at 100 and 290 K.

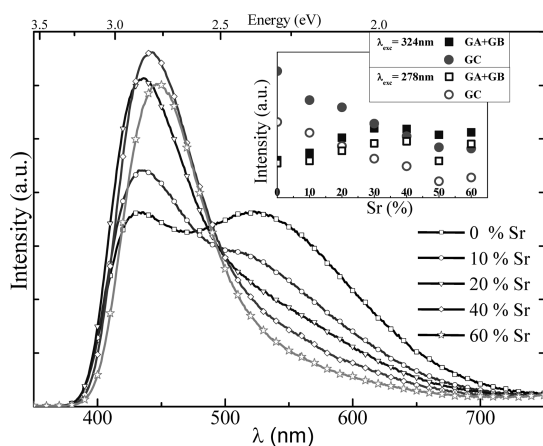


Figure 10. Influence of strontium substitution rate on the fluorescence of P-SrBASO:Eu1% materials ($\lambda_{\text{exc}} = 278$ nm). Insert: Evolution of GA+GB and GC intensities with Sr concentration for $\lambda_{\text{exc}} = 278$ and 324 nm.

reduced to the benefit of the Gc fluorescence by energy transfers. Beyond 3% of europium, concentration quenching is at work for both emissions. Concurrently, the maximum of the blue-violet band is red-shifted with Eu concentration because of the depletion of the higher excited-state via an energy transfer process.

3.2.3 Fluorescence of Sr-BASO:Eu Prepared under H_2/Ar Atmosphere. The substitution of Ba for Sr significantly affects the fluorescence spectrum of BASO in terms of relative ratio between the green and blue-violet emissions. As displayed in Figure 10, the emission spectra show a continuous decrease of the Gc band intensity with Sr rate, while the (GA + GB) bands intensity grows up at least up to a Sr concentration of 30 and 40% for excitation at 324 and 278 nm, respectively.

At this stage, we may wonder what chemical or steric factors govern the change in the emission spectra. Lesser energy transfers cannot be evoked to explain the observed trend because the number of luminescent centers inserted into the Sr-BASO host should not be modified versus Sr concentration. On the contrary, the location of Eu^{2+} cations might be strongly affected by Sr insertion. Consequently, the phenomenon may only lie in Sr-induced local distortions

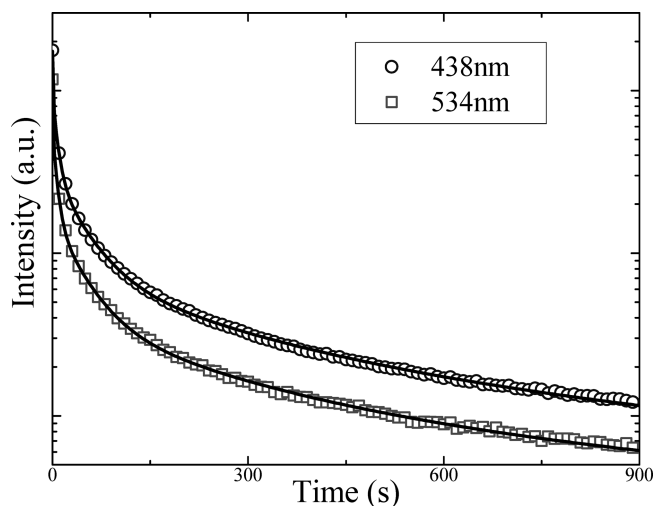


Figure 11. Room-temperature emission decay of 438 and 534 nm emissions from R-BASO:Eu1% fitted with five exponentials.

Table 4. Result of the Exponential Simulation of the 15 min Persistent Phosphorescence (R-BASO: Eu1%)

	438 nm	534 nm
I_{01}/I_{01}	1	1
τ_1 (s)	1.02(1)	0.82(1)
I_{02}/I_{01}	0.72	0.63
τ_2 (s)	7.33(1)	6.5(2)
I_{03}/I_{01}	0.28	0.21
τ_3 (s)	43(2)	41(2)
I_{04}/I_{01}	0.07	0.05
τ_4 (s)	210(20)	208(20)
I_{05}/I_{05}	0.03	0.02
τ_5 (s)	1050(100)	1080(110)

that favor the occupation of EuA and EuB sites by Eu at the expense of EuC ones.

3.2.4 Phosphorescence of BASO:Eu. After a brief UV illumination, the europium doped compounds R-BASO:Eu0.25 to 4% exhibit a white long afterglow that is perceived approximately for 10 min with a human eye after excitation is stopped. The room temperature emission decays of 438 and 534 nm bands are given in Figure 11 for R-BASO:Eu1% compound. The decay of both emissions can be decomposed into five exponentials as such

$$f(t) = y_0 + \sum_{x=1}^5 I_{0x} \exp\left(-\frac{t}{\tau_x}\right) \quad (1)$$

where y_0 is the signal noise, I_{0x} is the starting emission intensity associated with the depletion of trap x , and τ_x is the lifetime of the trapped state x at room temperature. Results are summed up in Table 4. According to the classic thermoluminescence scheme valid in insulators as long as $dn_c/dt \ll dn/dt$ and $n_c \ll n$, where n is the number of trapped charge carriers and n_c is the number of the charge carriers released in the conduction band, this suggests phosphorescence processes following first-order kinetics. Further investigations will be presented somewhere else to shed light on the thermoluminescence processes in BASO:Eu and the nature and depth of the traps. It is worth noticing that the 438 nm emission is always more intense than the 534 nm emission, along the afterglow decay at room temperature of BASO:1%Eu, (Figure 11). It is thus striking

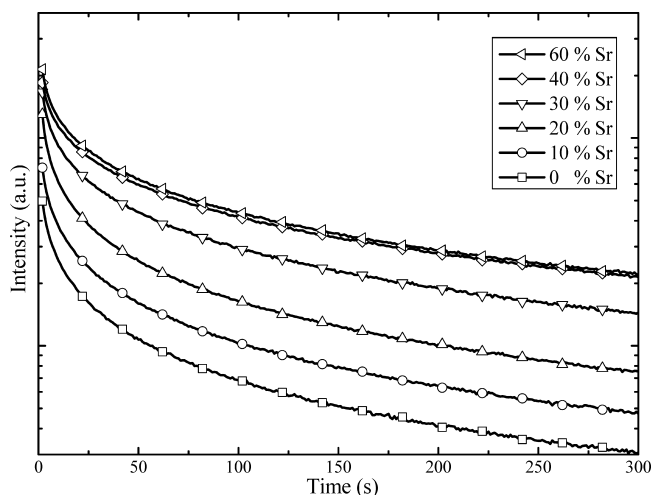


Figure 12. Influence of the strontium substitution on the 438 nm emission decay of P-SrBASO:Eu1% at room temperature. A similar trend is observed for the 534 nm emission.

to observe how much the overall features of the emission change, going from a fluorescence regime to a phosphorescence regime, the green luminescence being preponderant in the fluorescence mode at the expense of the blue-violet emission, while the inverse is observed in the phosphorescence mode. At this stage, on the basis of the similarity of the decay times of the two emissions, it can be reasonably supposed that equivalent traps are responsible for both emissions in phosphorescence.

In BASO, the perceived long afterglow intensity is maximum for europium concentrations ranging from 0.5% to 1%. These doping rates also correspond in fluorescence to the maximum of the GA+GB emission (insert in Figure 8). Moreover, the substitution of strontium for barium largely increases the persistent phosphorescence intensity of Sr-BASO:1Eu% compounds up to a strontium concentration of about 40% (Figure 12). This evolution is observed for both 438 and 534 nm (not shown here) isothermal emission decays. Beyond this strontium rate, the long afterglow intensity does not increase anymore. Consequently, as for the evolution with the europium doping rate, the persistent phosphorescence intensity with the strontium concentration goes along with the evolution of the fluorescence intensity of the blue band (GA+GB) in Figure 10.

4. Correlation between Crystal Structure and Fluorescence

The luminescence spectrum of Eu^{2+} -containing BASO and Sr-BASO materials can be decomposed in three Gaussian bands. Of course, it is tempting to associate each emission band with one of the three crystal sites of the barium in the structure $(\text{Ba,Sr})_{13-x}\text{Al}_{22-2x}\text{Si}_{10-2x}\text{O}_{66}$. Let us remember that the GA and GB bands have similar characteristics in terms of spectral width (0.24 and 0.34 eV) and position in energy (2.96 eV and 2.81 eV, respectively). In contrast, the GC emission band is much broader (0.59 eV) and emits at much lower energy (2.26 eV). From the crystallographic point of view, Ba1 and Ba2 sites display the same multiplicity (6c) and the same local symmetry (C_1). Moreover, both are surrounded by nonbridging tetrahedrons (T_{A} and T_{B}) with

terminal oxygen pointing toward Ba1 or Ba2. They are 8- and 7-fold coordinated with average Ba–O distances of 2.85 and 2.81 Å. On the contrary, Ba3 site exhibits a higher symmetry (C_3), a larger coordination (9), a lower multiplicity (2c) and occupancy rate of about 20%. Consequently, the similarity between the two GA and GB bands can be explained by the environment resemblance of the Ba1 and Ba2 sites. Thus, the two GA and GB fluorescence bands may be assigned to europium II cations randomly distributed over the Ba1 and Ba2 sites, while the emission band GC is assigned to europium II housed into the Ba3 site. Following this model, the lower energy emission GC originates from the europium II into the higher coordinated site Ba3. This is in contradiction with the classical model, which speculates that the higher coordination, the shorter the wavelength of the emission because of a lower crystal field splitting.²⁴ However, this argument may be rebutted on the basis of Akella et al. investigations on $\text{Ba}_2\text{Mg}(\text{BO}_3)_2\text{:Eu}$.²⁵ Indeed, this material contains one unique Ba site which is very similar in terms of coordination and interatomic distances to Ba3 site in BASO, that is, a $[\text{BaO}_9]$ polyhedra with Ba encapsulated between an $[\text{O}_6]$ hexagon and an $[\text{O}_3]$ triangle with short and long Ba–O distances, respectively. Europium II into the $\text{Ba}_2\text{Mg}(\text{BO}_3)_2$ structure exhibits a broad emission peaking at 608 nm with a large width of about 0.60 eV (Stokes shift of 1.36 eV). In view of the structural similarities and the overall feature of the emission peak, the attribution of the GC emission to europium in the Ba3 site of BASO appears reasonable, the wide width (and Stokes shift) being explained as a result of the large distribution of the Ba–O distances as did Dirksen et al. for $\text{Ba}_2\text{LiB}_5\text{O}_{10}\text{:Eu}$ for instance.²⁶

Surprisingly, the Ba3 site, which represents only one-seventh of the available site for Eu cation, induces a very intense green fluorescence band (GC), comparable or stronger to the blue emission (GA+GB) in BASO:Eu. As it is also the case at very low europium concentration, it seems unlikely that this originates from efficient energy transfers. More probably, and as shown by preliminary DFT calculations, a preferential location of Eu^{2+} into the higher-coordinated Ba3 site could be argued. With an ionic radius similar to the one of Eu^{2+} cations, we may suppose that Sr^{2+} cations also preferentially occupies the Ba3 site in Sr-BASO, as asserted also by preliminary DFT calculations. Consequently, both Eu and Sr ions will tempt to migrate toward Ba3 sites. Nevertheless, the evolution of the emission spectra of Sr-BASO:Eu1% materials (Figure 10) show an increase of (GA+GB) intensity at the expense of GC intensity when Sr concentration is increased. Naturally, we conclude that Sr^{2+} cations have a higher affinity for Ba3 sites than Eu^{2+} cations.

At the end, the noticeable reinforcement of the GA+GB emission at the expense of the GC emission of BASO:Eu0.25–4% samples going from fluorescence to phospho-

(24) Davalos, M. R.; Garcia, A.; Fouassier, C.; Hagenmuller, P. *J. Solid State Chem.* **1989**, *83*, 316–323.

(25) Akella, A.; Keszler, D. A. *Mater. Res. Bull.* **1995**, *30* (1), 105–111.

(26) Dirksen, G. J.; Blasse, G. *J. Solid State Chem.* **1990**, *92*, 591.

rescence, remains unclear. At first sight, this could be associated to traps specifically coupled to EuA and EuB, and EuC as suggested by Clabau et al.²⁷ Nevertheless, this may be rebutted at first sight in BASO and Sr-BASO because the decay times of the afterglows at 438 and 534 nm are very similar. Supplemental experiments are in progress to address this observation.

5. Conclusion

As initially proposed for Ba₁₃Al₂₂Si₁₀O₆₆ by Gebert,¹² the members of the (Ba,Sr)_{13-x}Al_{22-2x}Si_{10+2x}O₆₆ series crystallize in the *P*6₃ space group. A systematic deficiency in alkaline earth is noticed, the charge balance being then ensured via the partial substitution of Al for Si. Under a reducing atmosphere, Eu²⁺ cations can be stabilized and housed at the Ba sites. This goes along with the observation of a white

fluorescence and a white phosphorescence for Eu doping rate lower than 4% associated with two broad ⁸H-4f⁶5d¹ → ⁸S-4f⁷ emission bands at 534 and 438 nm. The high degree of tunability of the luminescence properties via the control of the Eu-doping rate and the substitution of Ba for Sr suggests potential applications as UV white LED, in particular because of the resemblance of the emission spectrum of some Sr-BASO:Eu materials with that of commercialized LED devices based on GaN blue chips coated with cerium-doped yttrium aluminum garnet. Investigations will be initiated soon to determine the performances of these materials as phosphor conversion UV-LED.

Supporting Information Available: Table showing the atomic positions of undoped R-BASO (Ba_{12.34}Al_{20.62}Si_{11.32}O₆₆) and P-BASO (Ba_{12.44}Al_{20.88}Si_{11.12}O₆₆). This material is available free of charge via the Internet at <http://pubs.acs.org>.

IC702240Q

(27) Clabau, F.; Rocquefelte, X.; Le Mercier, T.; Deniard, P.; Jobic, S.; Whangbo, M.-H. *Chem. Mater.* **2005**, *17*, 3904–3912.